

Micro-Vibration Analysis and Optimization of Aerostatic Bearing with Pocketed Orifice-Type Restrictor

Y. F. Li¹, Y. H. Yin^{1†}, H. Yang², X. E. Liu¹, J. Mo¹ and H. L. Cui²

¹*Institute of Systems Engineering, China Academy of Engineering Physics, Mianyang, 621900, China*

²*Institute of Mechanical Manufacturing Technology, China Academy of Engineering Physics, Mianyang, 621900, China*

†*Corresponding Author Email: yinyh@caep.ac.cn*

(Received April 22, 2017; accepted January 16, 2018)

ABSTRACT

For an aerostatic circular thrust bearing with a single pocketed orifice-type restrictor, the flow field in the bearing clearance is analyzed numerically, and the formation mechanism of the bearing micro-vibration is investigated. Through flow field analysis, the flow structures in the bearing clearance are discussed and classified. The formed vortex flow in flow field is analyzed, and the influence of the vortex flow on bearing dynamic stability related to micro-vibration is discussed. For each flow structure, the vortex flow always exists and induces the bearing micro-vibration. The Reynolds number is used to represent the degree of bearing micro-vibration and the rationality is verified. Based on the flow analysis results, the maximum Reynolds number in the bearing clearance flow field is taken as the optimization objective to reduce the micro-vibration amplitude, the approximate model for design optimization is established by using the radial basis functions method and the optimization methodology is illustrated. Several cases of optimization are carried out with different given bearing loads. Through optimization, the maximum Reynolds number is reduced greatly, which means the enhancement of the bearing dynamic stability. The optimization results show that in order to suppress the micro-vibration, the air supply pressure should be kept as small as possible, the small air pocket diameter and orifice diameter are also needed.

Keywords: Gas lubrication; Aerostatic bearing; CFD simulation; Micro-vibration; Dynamic stability; Design optimization.

NOMENCLATURE

a	radius of the permeable sphere	U_ϕ	micro-rotation component
b	radius of the solid sphere	ψ	stream function
\bar{v}	velocity vector	D	drag force
μ	dynamic viscosity	D_N	dimensionless drag
κ	vertex viscosity	$G_N(\zeta) \& H_N(\zeta)$	Gigenbauer functions
ω	microrotation vector	$K_{3/2}(\lambda r) \& I_{3/2}(\lambda r)$	modified Bessel functions
α, β, γ	gyro viscosity coefficients	T	stress tensor
p	pressure	Q	rate of flow

1. INTRODUCTION

Aerostatic bearings are widely used in ultra-precision machine tools due to their high motion accuracy. Several types of restrictors can be used in design of the aerostatic bearing such as the orifice-type, surface-compensated type and

porous type. Among them, the orifice-type restrictor has the widest application because of its simple manufacture and easy maintenance. Commonly, for the orifice-type restrictor, an air pocket may be added downstream of the orifice. Compared with the non-pocket type, the pocketed orifice-type restrictor makes the aerostatic bearing possess the better static

performances, e.g. larger load carrying capacity (LCC) or stiffness (Chen *et al.* (2006); Du *et al.* (2014)). Hence, the pocketed orifice type restrictor is adopted more widely. However, for the aerostatic bearing with pocketed orifice type restrictor (ABPOR), the occurrence of the micro-vibration decreases the bearing dynamic stability as described in Chen *et al.* (2011). For the micro-vibration of the ABPOR, some numerical and experimental research studies have been performed. In Aoyama *et al.* (2006), the flow field in the bearing clearance was simulated numerically and the occurrence of the micro-vibration was attributed to the formation of the vortex flow, the micro-vibration acceleration of the floating facility was measured experimentally and it was indicated that once the orifice-type restrictor with a round orifice outlet was applied instead of the sharp outlet, the generation of the vortex flow was suppressed, and the experimentally measured micro-vibration acceleration amplitude was decreased. The formation of turbulent flow also has an influence on the occurrence of the bearing micro-vibration, because vortexes with different scales always exist in the turbulent flow (Kawai *et al.* 2005; Yoshimura *et al.* (2012)). Commonly, the Reynolds number can be used to judge whether the flow is laminar or turbulent, the turbulent flow may occur when the Reynolds number becomes large enough in the flow field. The Reynolds number of the bearing clearance flow field of the ABPOR was changed by changing the air supply pressure, and the micro-vibration acceleration amplitude of the floating facility increased with the increase of the Reynolds number as described in Zhu *et al.* (2013). It means that with the larger Reynolds number, the micro-vibration amplitude of the bearing system is larger. This viewpoint is also supported by Zhang *et al.* (2007). While in these research studies, the relationship between the Reynolds number and micro-vibration of the ABPOR system was discussed only qualitatively, the quantificational relationship was not referred, so the Reynolds number cannot be used in bearing design yet to suppress the micro-vibration. From the previous research studies, the conclusion can be drawn that the vortex flow causes the fluctuation of pressure distribution in the bearing clearance flow field, resultantly, causes the fluctuation of LCC, and then the fluctuation of LCC induces the micro-vibration. Hence, the micro-vibration can be regarded as a kind of vortex-excited vibration. In modern manufacturing field, nanometer order and sub-nanometer order precision are commonly needed (Sato, 2006; Evans *et al.* 2006), hence, although the micro-vibration of the ABPOR is only at the nanometer order as discussed in Yoshimura *et al.* (2012), it can bring harm to bearing dynamic stability and will decrease machining and measuring precision of corresponding ultra-precision facilities. Consequently, it becomes essential to seek ways to suppress the micro-vibration of the ABPOR system. Because the occurrence of the micro-vibration is attributed to the formation of the vortex flow in the bearing clearance, getting a deep understanding of the formation process of the vortex flow and reducing the influence of the vortex flow may offer a way to suppress the micro-vibration. Design optimization offers a way to minimize the influence of the vortex flow, while the optimization modeling method should be studied. In Li *et al.* (2017), the aerostatic bearing with a single non-pocket orifice type restrictor was considered, the flow field was analyzed and the optimization modeling method was illustrated to reduce the influence

of the vortex flow, the radial basis functions (RBF) method as described in Hardy (1990) was used in establishing the approximate model for optimization which could achieve a high fitting accuracy.

With existence of the air pocket, the bearing flow field becomes more complicated for the ABPOR compared with the non-pocket situation, the flow structure and the formation process of the vortex flow should be investigated further. Besides, an effective design procedure for suppressing the micro-vibration is needed currently for the ABPOR. In this study, an aerostatic bearing with a single pocketed orifice type restrictor is considered. The formation mechanism of the vortex flow in the bearing clearance is illustrated, and the design strategy for suppressing the micro-vibration is proposed and verified. Firstly, the flow structure in the bearing clearance is analyzed and classified, the formation process of the vortex flow is illustrated, and the rationality of using the Reynolds number to represent the influence degree of the vortex flow is verified. The mathematical model of Reynolds number represented by bearing parameters is established by use of the RBF method. By establishing the approximate model, the influence of bearing parameters on the micro-vibration can be discussed in the quantificational way, which makes it possible to decrease the micro-vibration amplitude in bearing design stage. Then the optimization modeling method for the ABPOR is illustrated in detail, and the Reynolds number is considered as the design objective to suppress the vortex flow, i.e. to decrease the micro-vibration amplitude. Finally, several cases of optimization are conducted with different bearing loads and the results are compared and discussed.

2. Simulation Model and Governing Equations

The aerostatic circular thrust bearing with a single pocketed orifice-type restrictor is shown in Fig. 1. The bearing clearance includes the cylindrical air pocket and the air film. The working gas coming from an external source passes through the orifice and feeds into the air pocket, then the gas enters the air film and finally escapes from outside edge of the bearing. Bearing diameter D is 50mm, the orifice length l is 0.2mm. The cylindrical air pocket locates downstream of the orifice whose geometrical parameters include diameter U and depth V . The orifice diameter d , air pocket diameter U and depth V , together with the air supply pressure P_s (gauge pressure) are accounted as design variables. The design ranges are 0.1mm~0.2mm for d , 2mm~5mm for U , 0.1mm~0.2mm for V and 0.3MPa~0.6MPa for P_s . The air film thickness h varies with the given load. Part of the supply passage upstream of the orifice is also considered with the diameter of 3mm and the cone angle of 120°.

The working gas is compressible air and obeys the ideal gas law. The dynamic viscosity μ satisfies Sutherland's law as:

$$\frac{\mu}{\mu^*} = \left(\frac{T}{T^*}\right)^{3/2} \frac{T^* + S}{T + S} \quad (1)$$

where T is the gas temperature, $\mu^*=1.716 \times 10^{-5}$ Pa·s, $S=110.55$ K, and $T^*=273.11$ K.

The turbulent flow is considered in the numerical

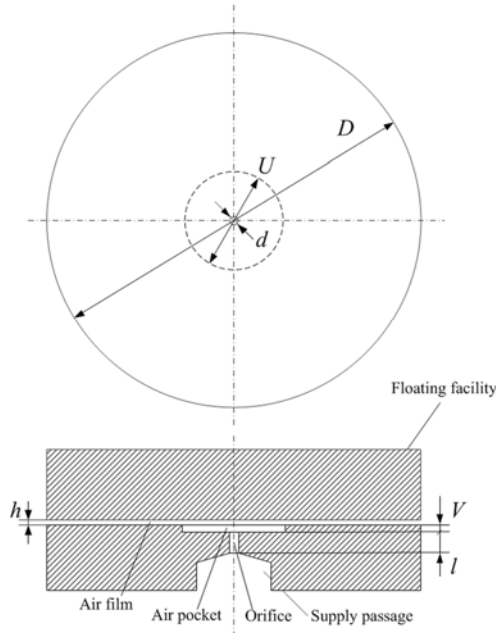


Fig. 1 Geometry model of aerostatic thrust bearing

simulation. The governing equations of the flow consist of continuity equation, momentum equations and energy equation. The equations are shown as Eq. (2) ~ Eq. (4).

$$\frac{\partial \bar{\rho}}{\partial t} + \frac{\partial(\bar{\rho} \tilde{u}_i)}{\partial x_i} = 0 \quad (2)$$

$$\frac{\partial(\bar{\rho} \tilde{u}_i)}{\partial t} + \frac{\partial(\bar{\rho} \tilde{u}_i \tilde{u}_j)}{\partial x_j} = -\frac{\partial \bar{p}}{\partial x_i} + \frac{\partial \bar{\sigma}_{ij}}{\partial x_j} + \frac{\partial[\bar{\rho}(\tilde{u}_i \tilde{u}_j - \widetilde{u_i u_j})]}{\partial x_j} + \frac{\partial(\bar{\sigma}_{ij} - \bar{\sigma}_{ij})}{\partial x_j} \quad (3)$$

$$\frac{\partial(\bar{\rho} \tilde{e} + \bar{\rho} \tilde{u}_i \tilde{u}_j / 2)}{\partial t} + \frac{\partial[(\bar{\rho} \tilde{e} + \bar{\rho} \tilde{u}_i \tilde{u}_j / 2 + \bar{p}) \tilde{u}_j]}{\partial x_j} = -\frac{\partial(\bar{\sigma}_{ij} \tilde{u}_i)}{\partial x_j} + \frac{\partial \bar{q}_j}{\partial x_j} + \hat{A} \quad (4)$$

where ρ is density of the gas, e is the total energy, u_i and u_j are velocity components, p is the pressure. $\bar{\sigma}_{ij}$ is the molecular viscous force which satisfies:

$$\bar{\sigma}_{ij} = \mu \left(\frac{\partial \tilde{u}_i}{\partial x_j} + \frac{\partial \tilde{u}_j}{\partial x_i} \right) \quad (5)$$

\bar{q}_j is the thermal conductivity which satisfies:

$$\bar{q}_j = -\lambda \frac{\partial \tilde{T}}{\partial x_j} \quad (6)$$

where λ is the thermal conductivity coefficient. \hat{A} in Eq. (4) can be represented as Eq. (7):

$$\hat{A} = -a_1 - a_2 - a_3 + a_4 + a_5 + a_6 \quad (7)$$

$a_1 \sim a_6$ are as Eq. (8) ~ Eq. (13).

$$a_1 = -\tilde{u}_i \frac{\partial[\bar{\rho}(\tilde{u}_i \tilde{u}_j - \widetilde{u_i u_j})]}{\partial x_j} \quad (8)$$

$$a_2 = \frac{\partial[\overline{eu_j} - \bar{e} \tilde{u}_j]}{\partial x_j} \quad (9)$$

$$a_3 = \bar{p} \frac{\partial \tilde{u}_j}{\partial x_j} - \bar{p} \frac{\partial \tilde{u}_j}{\partial x_j} \quad (10)$$

$$a_4 = \sigma_{ij} \frac{\partial \tilde{u}_i}{\partial x_j} - \bar{\sigma}_{ij} \frac{\partial \tilde{u}_i}{\partial x_j} \quad (11)$$

$$a_5 = \frac{\partial(\bar{\sigma}_{ij} \tilde{u}_i - \bar{\sigma}_{ij} \tilde{u}_i)}{\partial x_j} \quad (12)$$

$$a_6 = \frac{\partial(\bar{q}_j - \bar{q}_j)}{\partial x_j} \quad (13)$$

The subgrid stress $\tilde{\tau}_{ij}$ is defined as:

$$\tilde{\tau}_{ij} = \bar{\rho}(\tilde{u}_i \tilde{u}_j - \widetilde{u_i u_j}) \quad (14)$$

The superscript “-” means the spatial filter and “-” means the Favre filter in Eq. (2) ~ Eq. (14). The subgrid stress cannot be achieved directly by solving the governing equations and should firstly be modeled. Several turbulence models are offered for the modeling of the subgrid stress in fluid mechanics analysis as described in Kundu *et al.* (2012).

In this study, both steady and transient flow calculations are considered, the former is for analyzing flow structure and taking samples in establishing the approximate model for optimization, the latter is for analyzing the rationality of using the Reynolds number to represent bearing dynamic stability and verifying the optimization results.

3. FLOW FIELD ANALYSIS

3.1 Steady Flow Analysis

Through the steady flow calculation, static performances such as LCC, stiffness and mass flow rate can be calculated accurately (Chen *et al.* (2011); Aoyama *et al.* (2006)). Also, compared with the transient flow calculation, the computational expense of the steady flow calculation is rather less. So the steady flow calculation becomes the dominant numerical calculation in the design of aerostatic bearings.

The discussed flow field in the bearing clearance is simplified as a two-dimensional cylindrical symmetric one as shown in Fig. 2 according to the axisymmetric property of the flow geometry and boundary conditions. The bearing and air pocket surfaces are accounted as rigid walls which satisfy adiabaticity, impermeability and no-slip conditions, as Eq. (15) where x_l is along the normal direction of the surface, u_i^s is the velocity component at the surface. The pressure inlet condition is considered at the inlet position and the pressure equals the air supply pressure P_s , the pressure outlet condition is considered at the outlet and the pressure equals the atmospheric pressure P_0 . The pressure boundary conditions are as Eq. (16).

$$\frac{\partial T}{\partial x_l} = 0; \quad u_i = u_i^s \text{ at the bearing surfaces} \quad (15)$$

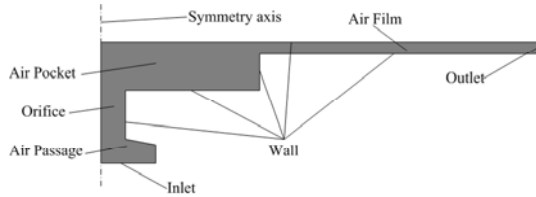


Fig. 2 Bearing clearance flow field and boundary conditions

$$\begin{cases} p = P_s & \text{at the inlet} \\ p = P_0 & \text{at the outlet} \end{cases} \quad (16)$$

The air pocket possesses a relatively larger volume than the orifice, so the flow characteristics are different from those of the aerostatic bearing with the non-pocket orifice type restrictor. The flow structure in the bearing clearance, especially in the air pocket, is complicated (Zhu *et al.* (2013); Li *et al.* (2015)) and is characterized by existence of numerous vortices with different scales. Also, the air pocket offers enough volume for development of the vortex flow. Hence, the turbulent flow is considered in the numerical simulation. The realizable $k-\epsilon$ model is used in the steady flow calculation as described in Chen *et al.* (2011). In order to verify the accuracy of the numerical calculation, the numerically calculated results of LCC are compared with experimental results in Aoyama *et al.* (2006) as shown in Fig. 3 where the relation of LCC versus air film thickness h is given. It can be seen that the experimental results and numerically calculated results are in good agreement, and the maximum error is less than 5% throughout $7\mu\text{m}$ to $15\mu\text{m}$ of h . Hence, the numerical calculation possesses enough accuracy.

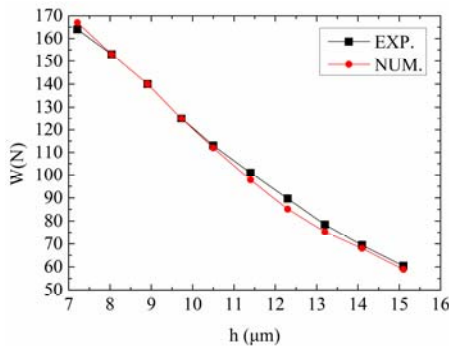
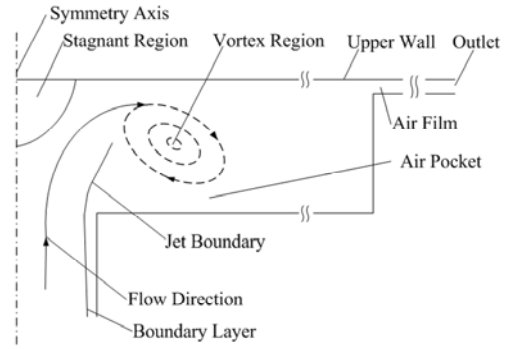
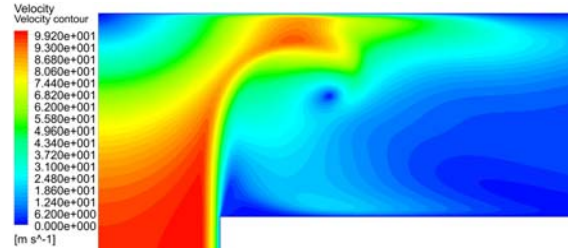


Fig. 3 Numerical and experimental results of LCC

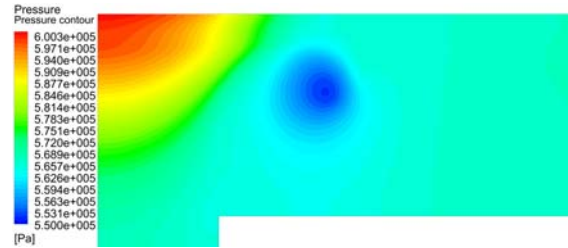
Through the steady flow calculation, two cases of flow structure in the air pocket are observed. In the first case, gas velocity stays subsonic in whole air pocket as shown in Fig. 4. The thickness of the boundary layer keeps increasing along the flow direction when the gas passes through the orifice. Because the volume of the air pocket is far larger than that of the orifice, the flow structure is similar to the free jet at the inlet of the air pocket with a clear jet boundary. While with the resistance of the thrust surface, i.e. the upper wall, there comes a stagnant region with high pressure as shown in Fig. 4a. Flow direction turns with the squeeze of the stagnant region, then the vortex forms. Velocity contour and pressure contour are shown in Figs. 4b and 4c for this case. Because the pressure always drops in the center of the vortex, the pressure contour can also be used to detect the formation of vortex as shown in Fig. 4c where the pressure drops in the center of the formed vortex.



a. Sketch map of flow structure



b. Velocity contour



c. Pressure contour

Fig. 4 Flow structure 1 in air pocket

In the second case, a supersonic region occurs near the inlet of the air pocket as shown in Fig. 5. The thickness of the boundary layer increases gradually from inlet to outlet of the orifice, resultantly, the effective area of cross section of the flow channel decreases gradually. While at the outlet of the orifice, the deflection of the jet boundary makes the effective area of cross section of the flow channel increase. Hence, for the effective area of cross section of the flow channel, a variation rule of former decrease and later increase appears. It generates a condition for the formation of the supersonic flow. The minimum cross section area of the flow channel locates at the outlet of the orifice, as section B-B in Fig. 5a. If the gas velocity is still subsonic at this position, then it will remain subsonic in the air pocket as discussed in the 1st flow structure. If the gas velocity reaches the sound velocity at section B-B, then with the disturbance of the deflection of the jet boundary at section B-B, expansion waves form and the gas velocity increases herein. Resultantly, the gas velocity gets faster than the sound velocity and the supersonic region occurs as shown in Fig. 5. Correspondingly, the pressure drops in this supersonic region downstream of expansion waves. Due to the high pressure in the stagnant region, the shock wave will form downstream of the supersonic region to make the pressure increase. Finally, due to the squeeze of the stagnant region, the flow direction turns and the vortex forms. The velocity contour and pressure contour of the 2st flow structure are shown as Figs. 5b and 5c.

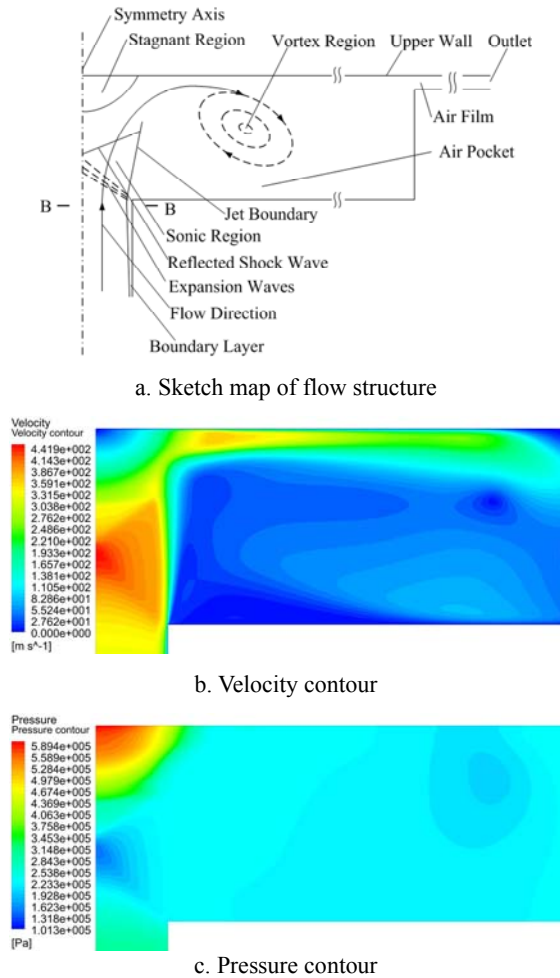


Fig. 5 Flow structure 2 in air pocket

It was referred that the formation of the vortex flow in the bearing clearance was harm to the bearing dynamic stability (Chen *et al.* (2011); Aoyama *et al.* (2006); Li *et al.* (2015)) for it would induce the micro-vibration. The micro-vibration amplitude should be reduced to improve the bearing dynamic stability. From the steady flow field simulation, it can be seen that for each flow structure, the vortex flow will form. Hence, it is essential to seek ways to reduce the influence of the vortex flow, namely to reduce the micro-vibration amplitude.

3.2 Transient Flow Analysis

Though the steady flow calculation is dominant in numerical simulation for the aerostatic bearing design (Chen *et al.* (2011), Aoyama *et al.* (2006)), with the increased demand of the machining and measuring precision of corresponding ultra-precision facilities, the time-varying properties should also be investigated to improve the bearing mechanical performances, especially the dynamic performances related to the bearing micro-vibration.

The formed vortexes in the air pocket can be detected, but the development and vanishing process of the vortexes cannot be simulated through the steady flow calculation, because the process is time-varying. Through the transient flow calculation, the vortex flow can be further investigated (Zhu *et al.* (2013); Li *et al.* (2015); Li *et al.* (2017)). When the vortex forms in the air pocket, it will move along the flow direction, and the new vortex

forms at the same position as that of the former one. Due to the effect of viscous dissipation, the formed vortexes will finally fade away. Because the pressure always drops at the center of the vortex, with the continuous generation and vanishing of vortexes, the pressure distribution in the air pocket varies with time. LCC is the integration of the pressure acting upon the thrust surface, so the time-varying pressure distribution will cause the fluctuation of LCC and then induce the micro-vibration.

Equivalent acceleration a_e defined in Li *et al.* (2017) was used as a direct measurement of the bearing micro-vibration degree in the transient flow calculation. a_e is expressed as Eq. (17) and its amplitude a_{eA} is expressed as Eq. (18).

$$a_e = (\tilde{W} - \bar{W})g / \bar{W} \quad (17)$$

$$a_{eA} = (W_{\max} - W_{\min})g / (2\bar{W}) \quad (18)$$

where \bar{W} and \tilde{W} are the time-average and the instantaneous values. W_{\max} and W_{\min} stand for the maximum value and the minimum value of LCC in the transient flow calculation, respectively.

Because it is necessary for the bearing to operate stably, the fluctuation of LCC should be controlled as small as possible. Hence, a_{eA} should be reduced to decrease the micro-vibration amplitude. For the case where $h=10\mu\text{m}$, $d=0.15\text{mm}$, $U=3.5\text{mm/s}$ and $P_s=0.45\text{MPa}$, the transient flow calculation is launched. The total time steps are 1000 and the time step size is 10^{-4}s . In order to get the more accurate vortex structure, the large eddy simulation method is applied. Figure 6 shows the velocity and pressure contours of the flow field in the air pocket. It can be seen from Fig. 6a that once the vortex forms, it moves along the flow direction, i.e. the radial direction of the bearing flow field, and finally vanishes due to the expansion of cross section area of the flow channel and the viscous dissipation effect. The vortexes exist in a torus region at millimeter level in the air pocket downstream of the orifice. The newly formed vortex is columnar vortex near the upper wall as described in session 3.1.

With the continuously generated and vanished vortexes, the pressure distribution in the flow field varies with time as shown in Fig. 6b. Because the air supply pressure is given as a constant value, the flow upstream of the formation place of the vortex is stable and nearly time-independent. Once the formed vortexes vanish, the flow becomes stable again. The influence of the vortex flow exists only in a small part of the flow field, and the majority part is stable and time-independent, so in the calculation of the static mechanical performances such as LCC or stiffness, the steady flow calculation possesses enough accuracy for the time-varying part is small enough to be neglected. However, in the analysis of the micro-vibration, the time-varying part should also be considered to have a more accurate understanding.

Figure 7 shows the fluctuation of a_e versus time. As mentioned above, the amplitude a_{eA} should be controlled as small as possible to reduce the micro-vibration.

The maximum Mach number was used to judge whether

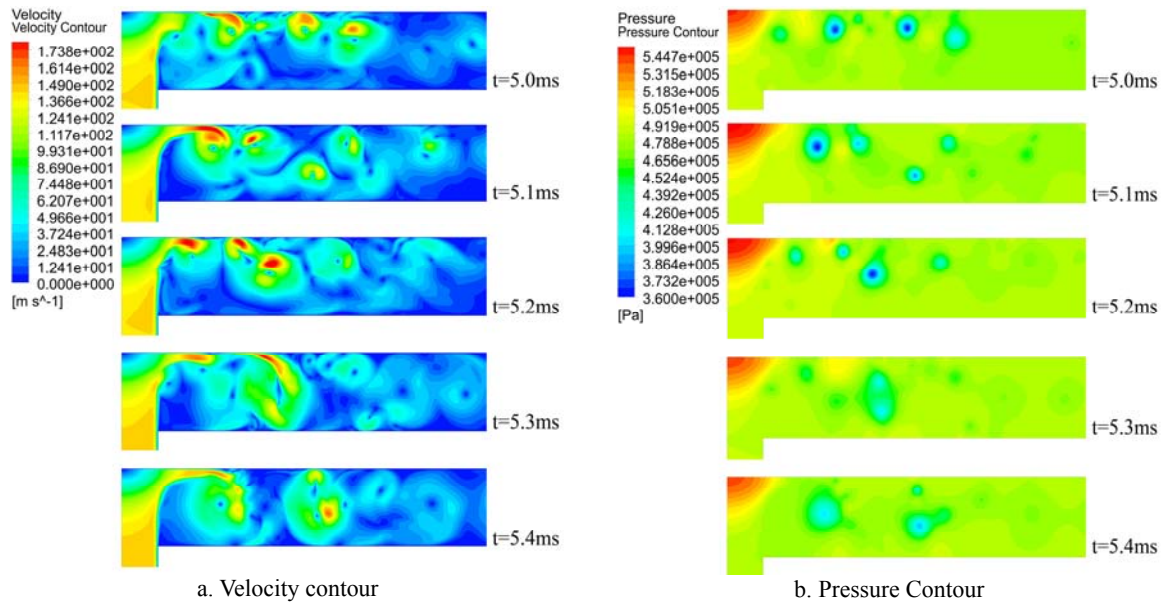


Fig. 6 Results of transient flow calculation

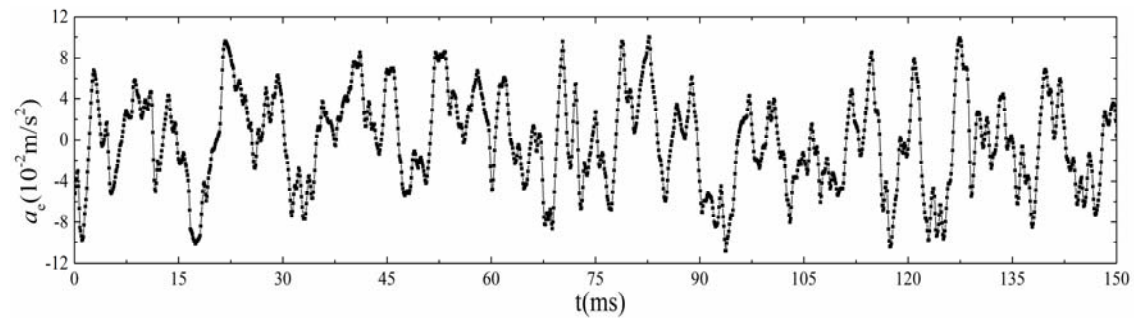


Fig. 7 Fluctuation of a_e versus time

the vortex flow existed or not in the air film of the aerostatic bearing with a single non-pocket orifice type restrictor in [Li *et al.* \(2017\)](#), it was concluded that the vortex flow existed only when the maximum Mach number is larger than 1. However, for the ABPOR as shown in Fig. 1, the vortex flow always exists, so the maximum Mach number is no longer suitable for application. In [Zhu *et al.* \(2013\)](#) and [Zhang *et al.* \(2007\)](#), it was referred that with a larger Reynolds number in the bearing flow field, the micro-vibration amplitude of the floating facility became larger, so the Reynolds number can be tried to represent the micro-vibration degree of the ABPOR system. The Reynolds number in [Eleshaky \(2009\)](#) is defined as Eq. (19) where \dot{m} means the gas mass flow rate and r is the radial coordinate whose origin is the center of the orifice. The Reynolds number can be calculated in whole bearing clearance flow field ($d/2 < r < D/2$), so a representative value of the Reynolds number should be chosen. The maximum value in the whole flow field is considered here and the related position commonly locates near the inlet of the air pocket ($r=d/2$). In latter discussion, Re denotes the maximum Reynolds number.

$$Re = \dot{m} / (2\pi r\mu) \quad (19)$$

In order to get a deep understanding of the micro-vibration, the relationship between Re and the micro-

vibration should be investigated in detail. The micro-vibration acceleration of the floating facility of an ABPOR was experimentally measured in [Li *et al.* \(2015\)](#), the same experimental cases are considered in this study. Firstly, the relationships between Re , a_e and experimentally measured micro-vibration acceleration amplitude a_A are discussed to illustrate the rationality of using Re to represent the bearing dynamic stability. Then based on the verification, Re is taken as the design objective in optimization to reduce the micro-vibration, i.e. to enhance the bearing dynamic stability, the optimization methodology is expounded, and several optimization cases are demonstrated in next session.

The bearing configuration in [Li *et al.* \(2015\)](#) is considered where D equals 40mm, U equals 6mm, h equals $12\mu\text{m}$, P_s equals 0.5MPa, d and V are changed. Through experiments, the micro-vibration acceleration amplitude a_A was achieved. Table 1 shows the comparison between Re , a_A and a_{eA} . It can be seen that Re varies monotonically with a_A or a_{eA} , which means that with a larger Re , a_{eA} and a_A become larger. Hence, to reduce the micro-vibration amplitude related to a_A , Re must be controlled as small as possible. It is reasonable to use Re as a benchmark of the dynamic stability related to the micro-vibration in the design of the ABPOR.

Table 1 Comparison between Re , a_A and a_{eA}

Case	Re	a_A (m/s ²)	a_{eA} (m/s ²)
$d=0.1\text{mm}, V=0.02\text{mm}$	1627	0.013	0.033
$d=0.1\text{mm}, V=0.06\text{mm}$	1644	0.016	0.039
$d=0.1\text{mm}, V=0.1\text{mm}$	1779	0.023	0.046
$d=0.15\text{mm}, V=0.1\text{mm}$	2539	0.043	0.129

It is worth mentioning that the transient flow calculation is more powerful in analyzing the bearing dynamic performances than the steady calculation, but it is far more time consuming. Hence, in the design optimization of the aerostatic bearing, using the steady flow calculation to perform the design optimization and using the transient flow calculation to verify the optimization results, especially the results related to dynamic performances, is an effective and practical way. The maximum Reynolds number Re locates near the inlet of the air pocket and the flow upstream of this position is stable and nearly time-independent, so Re is time-independent. For each case, the numerical results of Re achieved through steady and transient flow calculations are exactly the same. So the steady flow calculation is considered in later optimization to save the computational expense.

4. DESIGN OPTIMIZATION

4.1 Optimization Methodology

The aim of the optimization is to decrease the micro-vibration amplitude under the given bearing load. Firstly, the approximate model for optimization is established. Traditionally, the analytical formulas are used in analysis of performances such as LCC or stiffness of the aerostatic bearing with non-pocket orifice type restrictor. These theoretical formulas are derived under numerous hypotheses, such as one dimensional flow and laminar flow (Li *et al.* 2012). For the ABPOR, the flow structure is far more complicated and the turbulent flow exists in the bearing clearance, hence, the analytical formulas can no longer be developed and used, especially for the dynamic stability related to micro-vibration. Hence in this study, the approximate model is considered as the mathematical model of the bearing performance in optimization. The CFD simulation is applied in the sample taking. In CFD simulation, fewer hypotheses are considered and the turbulent flow can be calculated. Radial Basis Functions (RBF) method as described in Hardy (1990) was applied in establishing the approximate model for the aerostatic bearing optimization in Li *et al.* (2017) and could achieve a high fitting precision. So the RBF model is also considered here in establishing the approximate model.

As mentioned in flow field analysis in session 3, Re can be taken as the benchmark of the bearing dynamic stability related to the micro-vibration, and should be controlled as small as possible to reduce the micro-vibration amplitude. Hence, Re is set as the optimization objective, the minimum Re should be achieved under a given bearing load.

In design optimization, the design variable vector is set as \mathbf{x} . Firstly the sample points should be arranged and the

mechanical performances of each sample point should be calculated. Based on the theory of experiment design, the orthogonal experimental design method is considered to arrange the sample points. By use of this method, the detailed information of the design space can be achieved with relatively fewer sample points.

In the sample taking, the air film thickness h is exactly the response of the given bearing load, but it is also the geometry parameter of the flow field and should be given in CFD calculation for sample taking. For each sample point with certain combination of the bearing parameters, the bearing load is given and should be equal to LCC, h is determined firstly by a trial and reverse-directional way through a series of numerical simulations as described in Li *et al.* (2017). Once h is achieved, geometry of the flow field can be determined and the sampling values can be calculated.

In establishing the approximate model for optimization, the interpolation function of the RBF model is as Eq. (20).

$$f(\mathbf{x}) = \sum_{j=1}^N \alpha_j \phi_j(\mathbf{x}) + \alpha_{N+1} \tag{20}$$

where $f(\mathbf{x})$ is the interpolation function, $\phi_j(\mathbf{x}) = \phi(\|\mathbf{x} - \mathbf{x}_j\|)$ ($j=1,2,\dots,N$) is the radial basis function, $\mathbf{x}_1, \mathbf{x}_2, \dots, \mathbf{x}_N$ are sample points. $\alpha_1, \alpha_2, \dots, \alpha_{N+1}$ are unknown interpolation expansion coefficients. y_i is corresponding sampling value related to i th sample point. $\alpha_1, \alpha_2, \dots, \alpha_{N+1}$ can be obtained by substituting sample points and corresponding sampling values into Eq. (20) and solving Eq. (21).

$$\begin{cases} \sum_{j=1}^N \alpha_j \phi_j(\mathbf{x}_i) + \alpha_{N+1} = y_i, i = 1, \dots, N \\ \sum_{j=1}^N \alpha_j = 0 \end{cases} \tag{21}$$

The variable power spline basis function is used here as the radial basis function, the definition is as Eq. (22).

$$\phi(\mathbf{x}) = \|\mathbf{x} - \mathbf{x}_j\|^c \tag{22}$$

where $\|\mathbf{x} - \mathbf{x}_j\|$ is the Euclidian distance, c is the shape function factor which can be got by minimizing sum of the errors in the interpolation. The fitting accuracy of the approximate model should be verified.

Each design variable is normalized through Eq. (23) before establishing the approximate model. x stands for any component of the design variable vector \mathbf{x} , x_{\max} and x_{\min} are its upper and lower bounds, respectively.

$$\bar{x} = (x - x_{\min}) / (x_{\max} - x_{\min}) \tag{23}$$

The mathematical model of the optimization is as Eq. (24).

$$\begin{aligned} \min \quad & Re(\mathbf{x}) \\ \text{s.t.} \quad & \mathbf{x} \in \mathbf{E} \end{aligned} \tag{24}$$

where \mathbf{E} is the feasible design field. The sequential quadratic programming (SQP) algorithm is applied in this study to seek the optimum point. The detail of SQP algorithm is discussed in Nocedal *et al.* (2006). SQP

algorithm is especially effective in nonlinearly constrained optimization. The basic idea of this algorithm is to turn the primal optimization problem into a series of quadratic programming sub-problems and progressively seek the optimum design point.

4.2 Optimization Cases

In the present optimization, design variables include d , P_s , U and V . Hence, the design variable vector x is (d, P_s, U, V) . Firstly the interpolation function of $Re(x)$ should be determined by using Eq. (20). According to the theory of the orthogonal experimental design, the

orthogonal layout $L_{98}(7^4)$ with 4 factors and 7 levels is designed for taking samples in the feasible design field E as shown in Eq. (25). The factors and levels are determined as shown in Table 2.

$$\begin{aligned} d &\in (0.1\text{mm}, 0.2\text{mm}) \\ P_s &\in (0.3\text{MPa}, 0.6\text{MPa}) \\ U &\in (2\text{mm}, 5\text{mm}) \\ V &\in (0.1\text{mm}, 0.2\text{mm}) \end{aligned} \tag{25}$$

Several optimization cases are considered with different given bearing loads. The loads include 100N, 120N and 150N. For each optimization case, the sample values are

Table 2 Factors and levels of the orthogonal layout $L_{98}(7^4)$

Factor	level 1	level 2	level 3	level 4	level 5	level 6	level 7
$d(\text{mm})$	0.10	0.12	0.14	0.15	0.16	0.18	0.20
$P_s(\text{MPa})$	0.30	0.35	0.40	0.45	0.50	0.55	0.60
$U(\text{mm})$	2.00	2.50	3.00	3.50	4.00	4.50	5.00
$V(\text{mm})$	0.10	0.12	0.14	0.15	0.16	0.18	0.20

calculated and the approximate model is established. In establishing the approximate model, the fitting accuracy is verified by R_a^2 factor, the factor is larger than 0.95 in each case, which indicates a high fitting accuracy. By establishing the approximate model, the quantificational relationship between Re and (d, P_s, U, V) can be achieved. For simplicity, the expressions are omitted here. Figure 8 shows the relationship of Re versus normalized d and P_s when U equals 3.5mm, V equals 0.15mm and the given bearing load equals 100N. It can be seen in Fig. 8 that with the increase of the air supply pressure or the orifice diameter, Re increases. The rule indicates that the gas mass flow rate has a dominant influence on Re . Gas mass flow rate increases with increase of the air supply pressure, so Re increases according to Eq. (19). The cross section area of the orifice is increased by increase of the diameter, the air-lock effect is decreased and the gas mass flow rate increases in case of Fig. 8, and Re increases resultantly.

The SQP algorithm is applied and the termination accuracy is set as 10^{-6} . The optimization results are shown in Table 3. For each optimization case, a_{eA} is also calculated for verification of the optimization results.

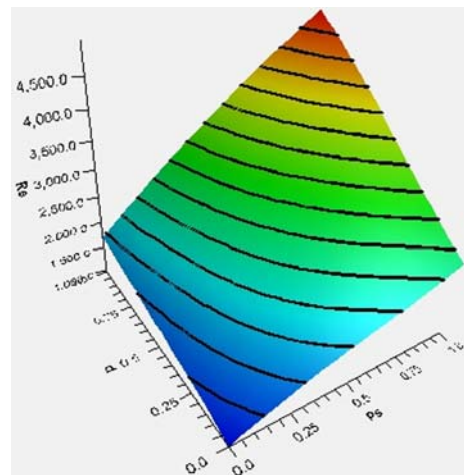


Fig. 8 Re versus d and P_s

It can be seen in Table 3 that each optimum point occurs with the minimum air supply pressure, which accords with the influence rule as shown in Fig. 8. It means that the air supply pressure should be kept as small as possible to reduce the micro-vibration amplitude. A small air pocket diameter should also be adopted. The comparison between Re and a_{eA} verifies the rationality of

Table 3 Optimum results

Load	Objective	d (mm)	U (mm)	V (mm)	P_s (MPa)	h (μm)	Re	a_{eA} (10^{-2}m/s^2)
100N	Initial value	0.15	3.5	0.150	0.45	16.50	2512	10.055
	Minimum Re	0.10	2.0	0.125	0.30	10.28	901	4.242
120N	Initial value	0.15	3.5	0.150	0.45	15.40	2474	9.185
	Minimum Re	0.10	2.0	0.130	0.30	8.10	589	1.773
150N	Initial value	0.15	3.5	0.150	0.45	13.65	2320	8.332
	Minimum Re	0.10	2.0	0.134	0.30	3.60	91	0.031

using Re to represent bearing dynamic stability again, because the smaller Re is, the smaller a_{eA} becomes. Through optimization, Re is reduced greatly. For the case that the given bearing load equals 100N, Re declines by 64% and a_{eA} declines by 58%, for the case that the given bearing load equals 120N, Re declines by 76% and a_{eA} declines by 81%, and for the case that the given bearing load equals 150N, Re declines by 96% and a_{eA} declines by 99%. It is indicated that with a larger given load, both Re and a_{eA} decrease more. From the comparison between initial value of different cases, it can be seen that the larger given bearing load brings smaller Re or a_{eA} , when the given bearing load increases to 150N from 100N, Re declines by 8% and a_{eA} declines by 17%, which indicates that a larger given bearing load can bring the better dynamic stability. However, it should be mentioned that in the feasible design field as shown in Eq. (25), the LCC offered by the bearing has an upper bound (Li *et al.* 2017), so the given bearing load should always be less than the maximum LCC whose value is about 400N in this study.

5. CONCLUSIONS

The flow field in the bearing clearance of an aerostatic thrust bearing with a single pocketed orifice-type restrictor is studied. The flow structure is illustrated through the steady flow simulation. Transient flow simulation is considered further to verify the rationality of using the maximum Reynolds number Re to represent the bearing dynamic stability related to micro-vibration. Based on the analysis, the mathematical model of optimization is established. Several cases of bearing loads are considered in design optimization. For each case, the optimum design with the minimum Re is achieved to improve the bearing dynamic stability. The optimum results are compared and discussed. From the study, the following conclusions can be drawn:

Two different flow structures exist in the air pocket, with or without a supersonic region at the inlet of the air pocket. Whether the supersonic region exists or not, vortex flow will form and can cause the micro-vibration of the floating facility. Re can be used to represent the bearing dynamic stability related to micro-vibration, and should be controlled as small as possible to reduce the micro-vibration amplitude.

In order to achieve a well bearing dynamic stability with smaller micro-vibration amplitude, the air supply pressure should be kept as small as possible and the air pocket diameter should be small enough. It is also necessary for the bearing to operate under a relatively large given load to improve the bearing dynamic stability, but the load should be less than the maximum LCC in feasible design field. Because the decrease of the air supply pressure may decrease the bearing static performances in some situations, the multi-objective optimization method can be used in the future in the bearing design to achieve the optimization result which balances both static and dynamic performances.

ACKNOWLEDGMENT

The work described in this paper was supported by the key subject "Computational Solid Mechanics" of the China academy of engineering physics and key project of science and technology of the China academy of engineering physics (9120602).

REFERENCES

- Aoyama, T., Y. Kakinuma, and Y. Kobayashi (2006). Numerical and experimental analysis for the small vibration of aerostatic guideways. *CIRP Ann-Manuf Technol* 55, 419-422.
- Chen, X. D. and X. M. He (2006). The effect of the recess shape on performance analysis of the gas-lubricated bearing in optical lithography. *Tribology Int* 39, 1336-1341.
- Chen, X. D., H. Chen, X. Luo, Y. X. Ye, Y.T. Hu, and J.Q. Xu (2011). Air vortices and nano-vibration of aerostatic bearings. *Tribol Lett* 42, 179-183.
- Du, J. J., G. Q. Zhang, T. Liu, and S. To (2014). Improvement on load performance of externally pressurized gas journal bearings by opening pressure-equalizing grooves. *Tribology Int* 73, 156-166.
- Eleshaky M. E. (2009). CFD investigation of pressure depressions in aerostatic circular thrust bearings. *Tribology Int* 42, 1108-1117.
- Evans, J. W., B. Macintosh, L. Poyneer, K. Morzinski, S. Severson, D. Dillon, D. Gavel, and L. Reza (2006). *Demonstrating sub nm closed loop MEMS flattening*. *Opt Express* 14, 5558-5570.
- Hardy R. L. (1990). Theory and applications of the multiquadric-biharmonic method 20 years of discovery 1968-1988. *Comput Math. Applic* 19(8-9), 163-208.
- Kawai, T., K. Ebihara, and Y. Takeuchi (2005). Improvement of machining accuracy of 5-axis control ultraprecision machining by means of laminarization and mirror surface finishing. *CIRP Ann-Manuf Technol* 54, 329-332.
- Kundu, P. K., I. M. Cohen, and D. R. Dowling (2012). *Fluid mechanics*, Elsevier, Singapore.
- Li, Y. F., Y. H. Yin, H. Yang, X. E. Liu, J. Mo, and H. L. Cui (2017). Modeling for optimization of circular flat pad aerostatic bearing with a single central orifice-type restrictor based on CFD simulation. *Tribology Int* 109, 206-216.
- Li, Y. T. and H. Ding (2012). A simplified calculation method on the performance analysis of aerostatic thrust bearing with multiple pocketed orifice-type restrictors. *Tribology Int* 56, 66-71.
- Li, Y. T., J. Y. Zhao, H. X. Zhu, and Y.X. Lin (2015). Numerical analysis and experimental study on the microvibration of an aerostatic

- thrust bearing with a pocketed orifice-type restrictor. *Proc. IMechE Part J: J Eng Tribology* 229(5), 609-623.
- Nocedal, J. and S. J. Wright (2006). Numerical optimization, Springer, New York, USA.
- Sato K. (2006). Trend of precision positioning technology. *ABCM Symp Ser Mechatron* 2, 739-750.
- Yoshimura, T., T. Hanafusa, T. Kitagawa, T. Hirayama, T. Matsuoka, and H. Yabe (2012). Clarifications of the mechanism of nano-fluctuation of aerostatic thrust bearing with surface restriction. *Tribology Int* 48, 29-34.
- Zhang, M., Y. Zhu, G. Ren, G. Duan, and G. Gao (2007). Finite element and experimental analysis on micro-vibration of ultra-precision air bearing linear motion stage and methods of its elimination. *First International Conference on Integration and Commercialization of Micro and Nanosystems*, 83-87.
- Zhu, J. C., H. Chen, and X. D. Chen (2013). Large eddy simulation of vortex shedding and pressure fluctuation in aerostatic bearings. *J. Fluids. Struct* 40, 42-5.